Supplement of Earth Syst. Sci. Data, 18, 7719–7742, 2026
https://doi.org/10.5194/essd-18-7719-2026-supplement
© Author(s) 2026. CC BY 4.0 License.



Open Access Earth System Science Data

Supplement of

FineKarstAGB: a 30 m resolution aboveground biomass dataset for Southwest China derived by upscaling plot-level inventory using sub-meter GaoFen satellite data

Yixiang Li et al.

Correspondence to: Yongqing Bai (baiyq@aircas.ac.cn)

The copyright of individual parts of the supplement might differ from the article licence.

Sect. S1 Growth-slowdown sensitivity analysis

To quantify the potential AGB change over the remaining temporal gap without assuming a constant long-term growth rate, we fitted a growth-slowdown model to the non-anomalous NFI8–NFI9 pairs. The response was annual AGB change, and the predictor set comprised NFI8 AGB, stand age, forest type, forest origin, province, elevation, and slope. Stand age at NFI8 was obtained by subtracting the five-year inventory interval from the recorded NFI9 age, with a lower bound of one year. The model can be written as

$$\frac{\Delta \mathrm{AGB}_i}{\Delta t} = f_s[\log(\mathrm{AGB}_{\mathrm{NFI8},i} + 1)] + f_a(\mathrm{age}_i) + \boldsymbol{\beta}^{\mathsf{T}} \mathbf{X}_i + \varepsilon_i. \tag{S1}$$

where f_s and f_a were represented by cubic B-spline bases with five knots, and $\mathbf{X}_i$ contained forest type and origin, province, elevation, and slope. The spline coefficients and covariate effects were estimated using ridge regression (penalty parameter = 20). Target values were winsorized at the 2.5th and 97.5th percentiles within each training fold, and model performance was evaluated using five-fold 0.25° spatial-block cross-validation. For the 6-, 8-, and 10-year sensitivity scenarios, the fitted annual increment was recalculated after updating AGB and age at each one-year step:

$$\begin{aligned} \mathrm{AGB}_{i,t+1} &= \max\left[0,\ \mathrm{AGB}_{i,t} + \widehat{g}\left(\mathrm{AGB}_{i,t}, \mathrm{age}_{i,t}, \mathbf{X}_i\right)\right], \\ \mathrm{age}_{i,t+1} &= \mathrm{age}_{i,t} + 1. \end{aligned} \tag{S2}$$

This recursive implementation allows the predicted increment to change as stands age and biomass accumulates, avoiding direct linear extrapolation of the NFI8–NFI9 growth rate. GaoFen-derived NDVI, crown coverage, canopy height, and CSMF-Net predictions were not used in either the temporal classification or the growth-slowdown model.

Table S1. Provincial statistics of image tiles and tree counts in Southwest China.

Province	Image tiles	Tree counts (billion)
Yunnan	5208	7.68
Guizhou	2392	5.25
Guangxi	3075	3.85
Hunan	2973	4.23
Total	13648	21.01

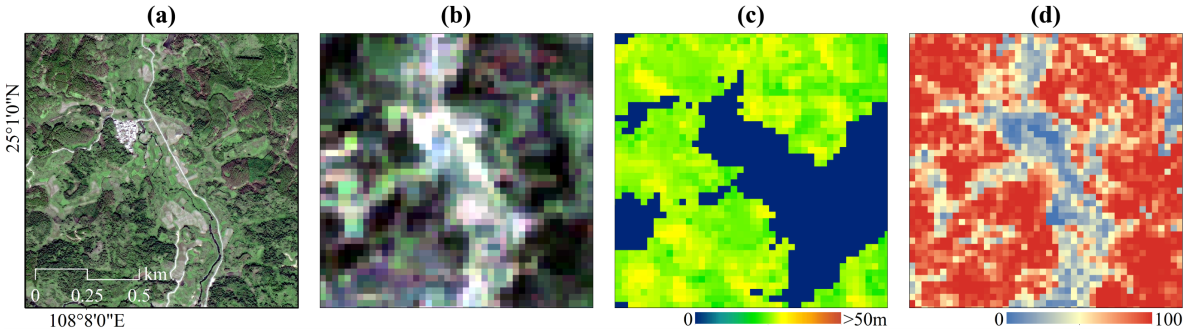


Figure S1. Comparison of remote-sensing imagery and forest-parameter products at different spatial resolutions in Southwest China. (a) GaoFen imagery (0.8 m), (b) Landsat imagery (30 m), (c) forest canopy height (Liu et al., 2022b) (30 m), and (d) tree cover (Cai et al., 2024a) (30 m).

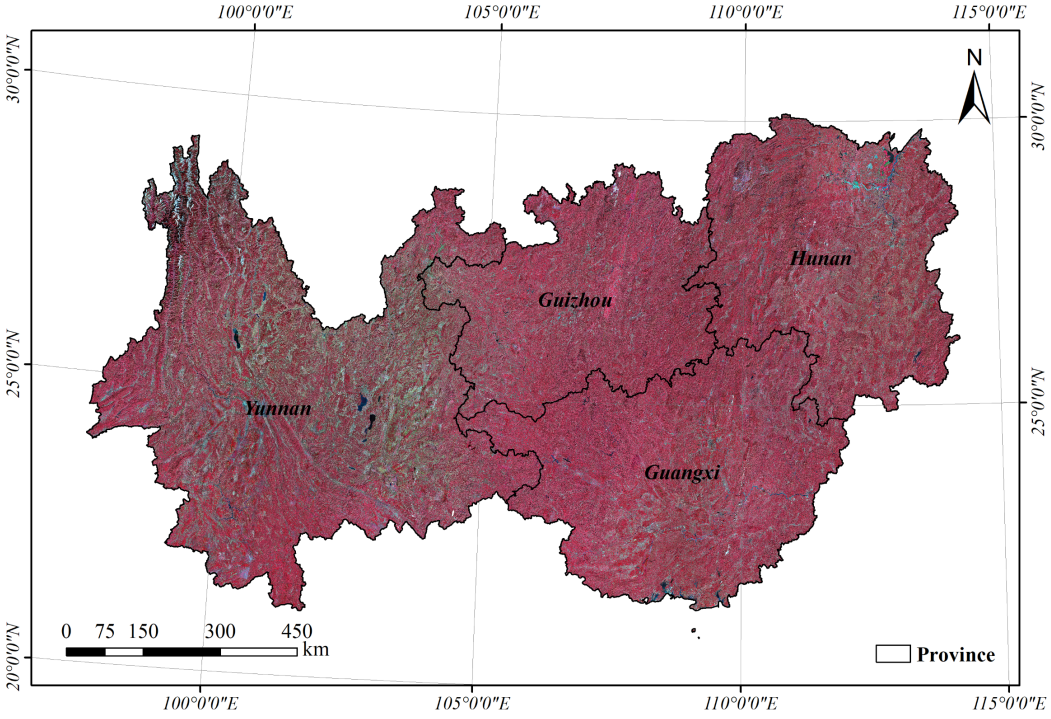


Figure S2. Spatial mosaic of the processed GF-2/GF-7 GaoFen imagery covering the four-province study area. The mosaic contains 13,648 image tiles and is displayed using the near-infrared, red, and green bands.

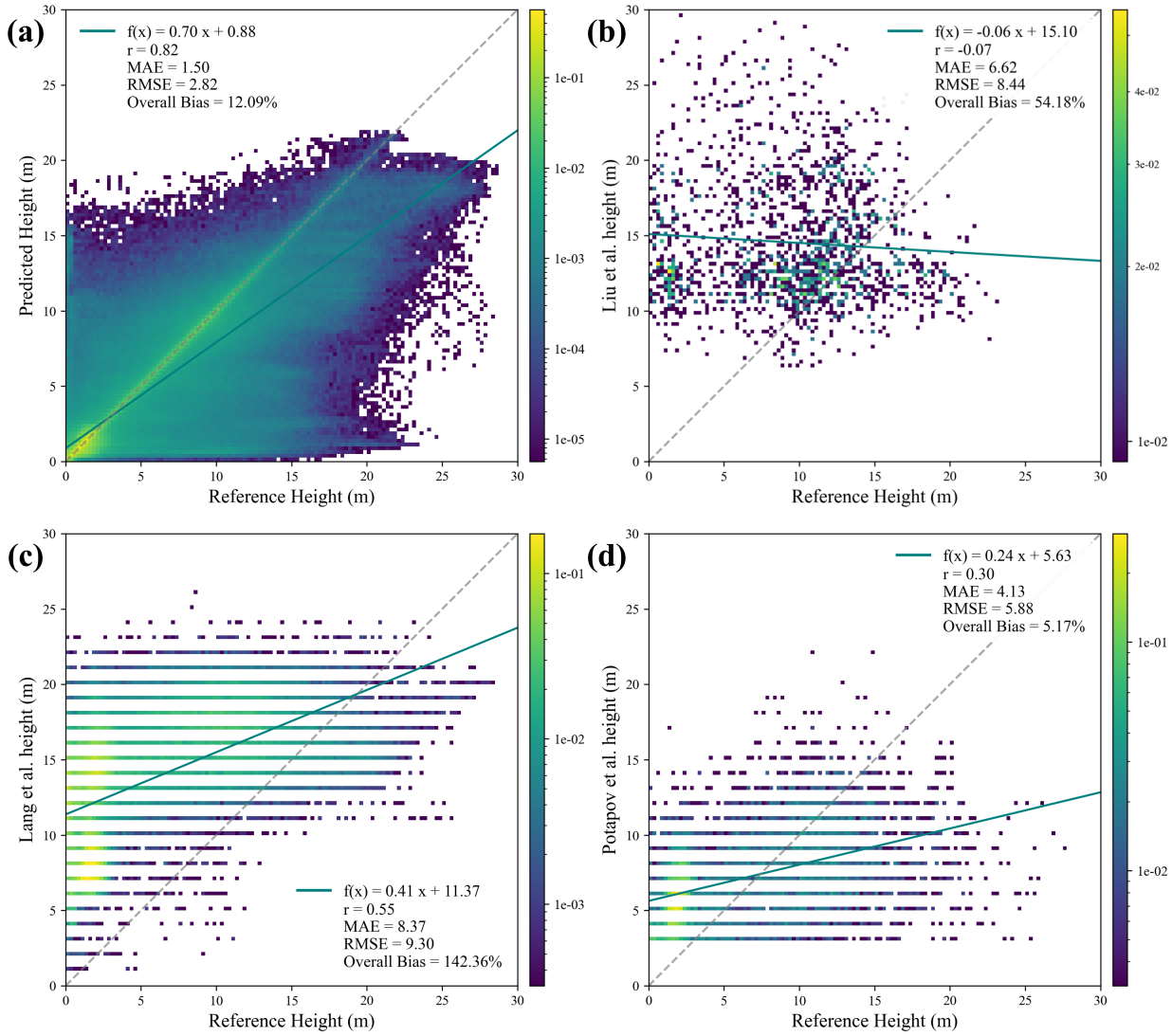


Figure S3. Comparison of canopy-height products with independent UAV LiDAR-derived CHMs from LIDARNET (http://lidar.pku.edu.cn). (a) GaoFen-derived canopy-height dataset used in this study. (b) National canopy-height product of Liu et al. (2022b). (c) Global canopy-height product of Lang et al. (2023). (d) Global forest-canopy-height product of Potapov et al. (2021). The UAV LiDAR CHMs were aggregated to the native resolution of each product before evaluation.

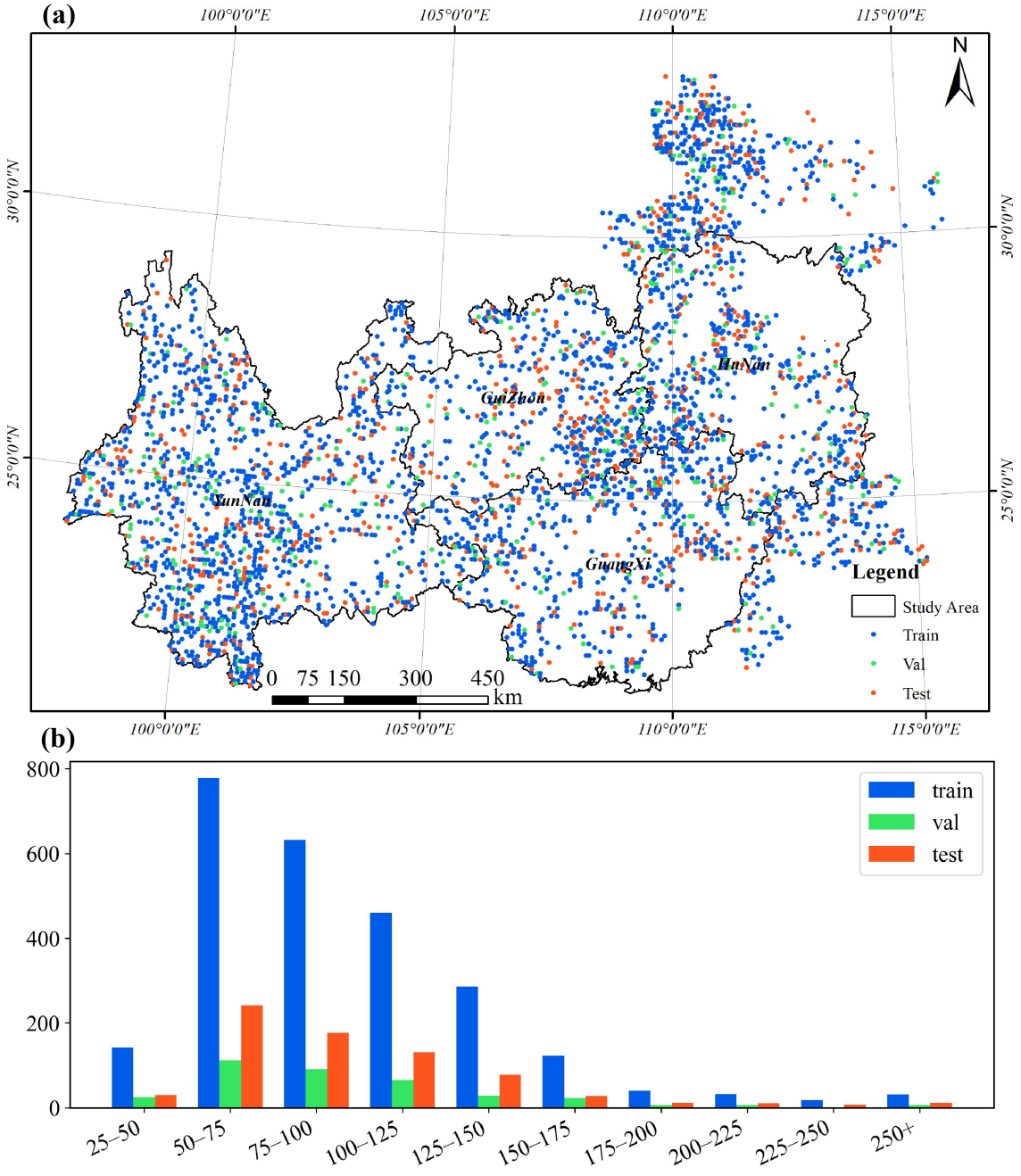


Figure S4. Overview of the National Forest Inventory (NFI) data. (a) Spatial distribution of the NFI plots. (b) Frequency distributions of the training, validation, and test samples by AGB interval.

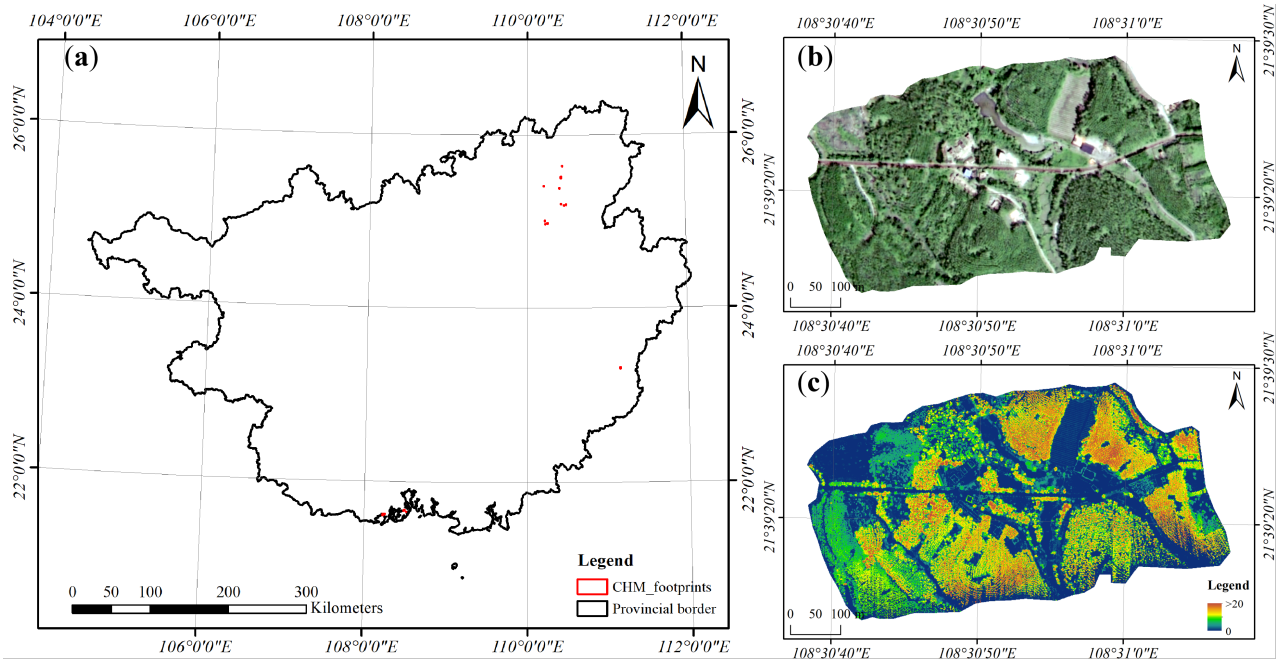


Figure S5. Spatial distribution and example of the UAV LiDAR data used in this study. (a) Distribution of the 18 UAV LiDAR datasets across Guangxi Province, including Guilin ($n = 10$), Fangchenggang ($n = 6$), and Wuzhou ($n = 2$). (b) GaoFen imagery of a representative UAV LiDAR site. (c) Corresponding UAV LiDAR-derived canopy-height model. Panels (b) and (c) show the same spatial extent. The UAV LiDAR data cover approximately 1,208 ha in total, and the CHMs have a spatial resolution of 0.05 m.

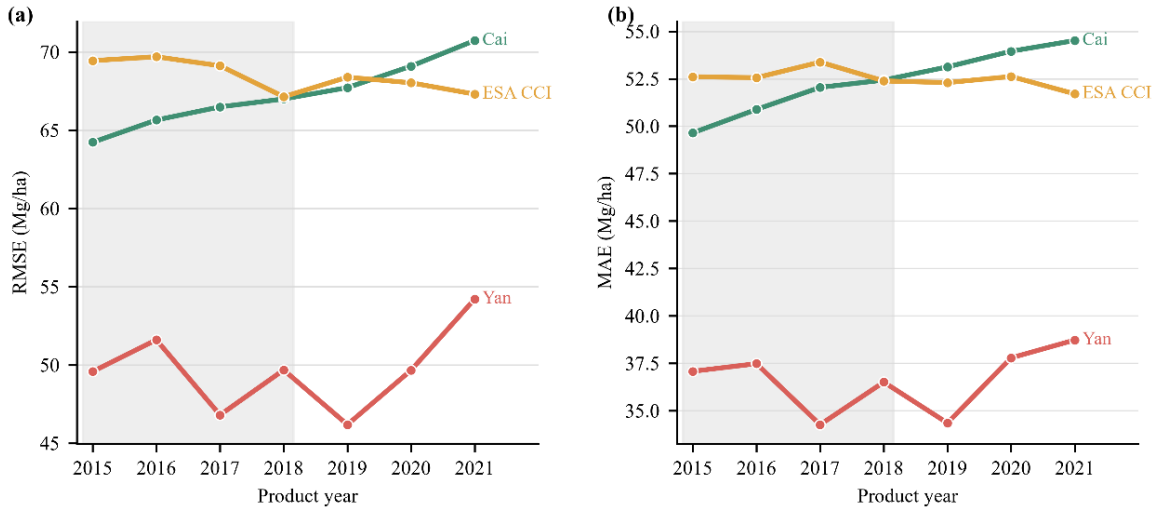


Figure S6. Sensitivity of the cross-product evaluation to product year. Annual (a) RMSE and (b) MAE from 2015 to 2021. For each product, all annual estimates were evaluated using the same product-specific set of NFI test plots with valid estimates throughout the period. The gray bands indicate the common 2015–2018 interval overlapping most of the NFI observation period. Although both metrics varied among product years, the broad differences among the products persisted throughout 2015–2021.

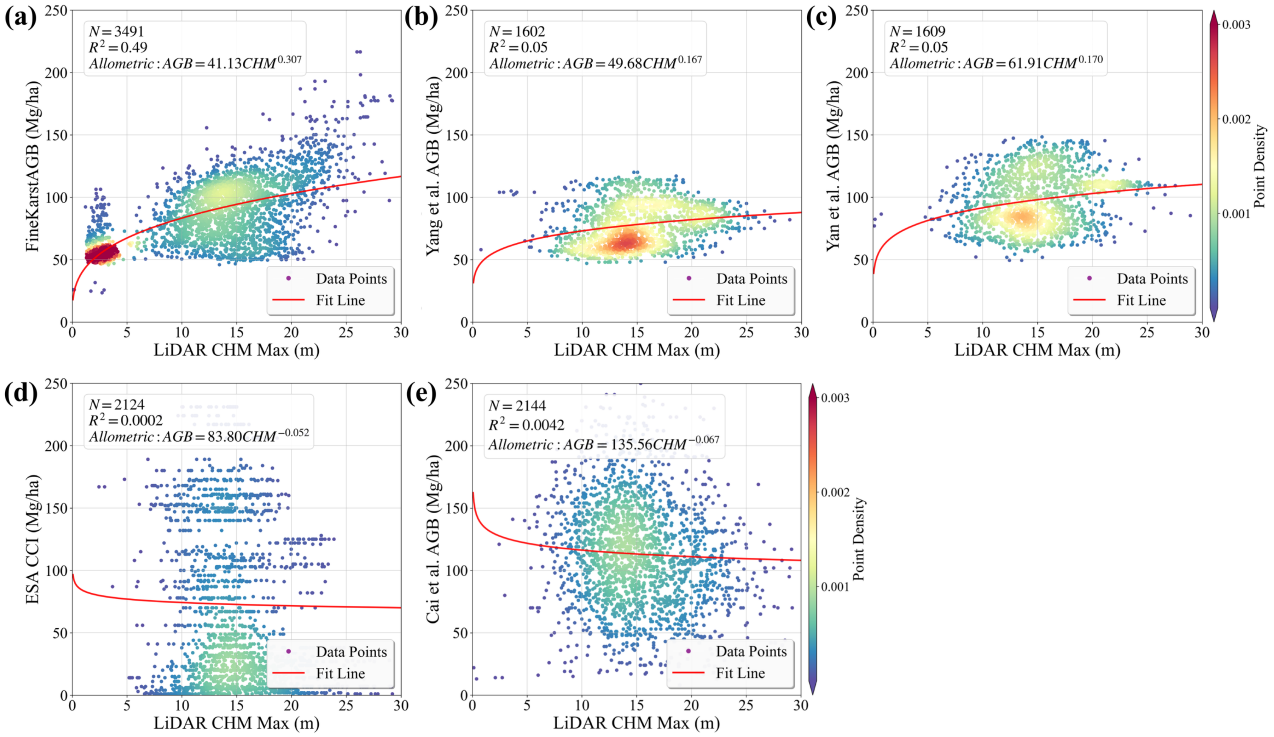


Figure S7. Structural-consistency assessment of the AGB datasets against maximum UAV LiDAR-derived canopy height. Results are shown for (a) FineKarstAGB, (b) Yang et al. (2023), (c) Yan et al. (2023a), (d) ESA CCI (Santoro and Cartus, 2025), and (e) Cai et al. (2024b).

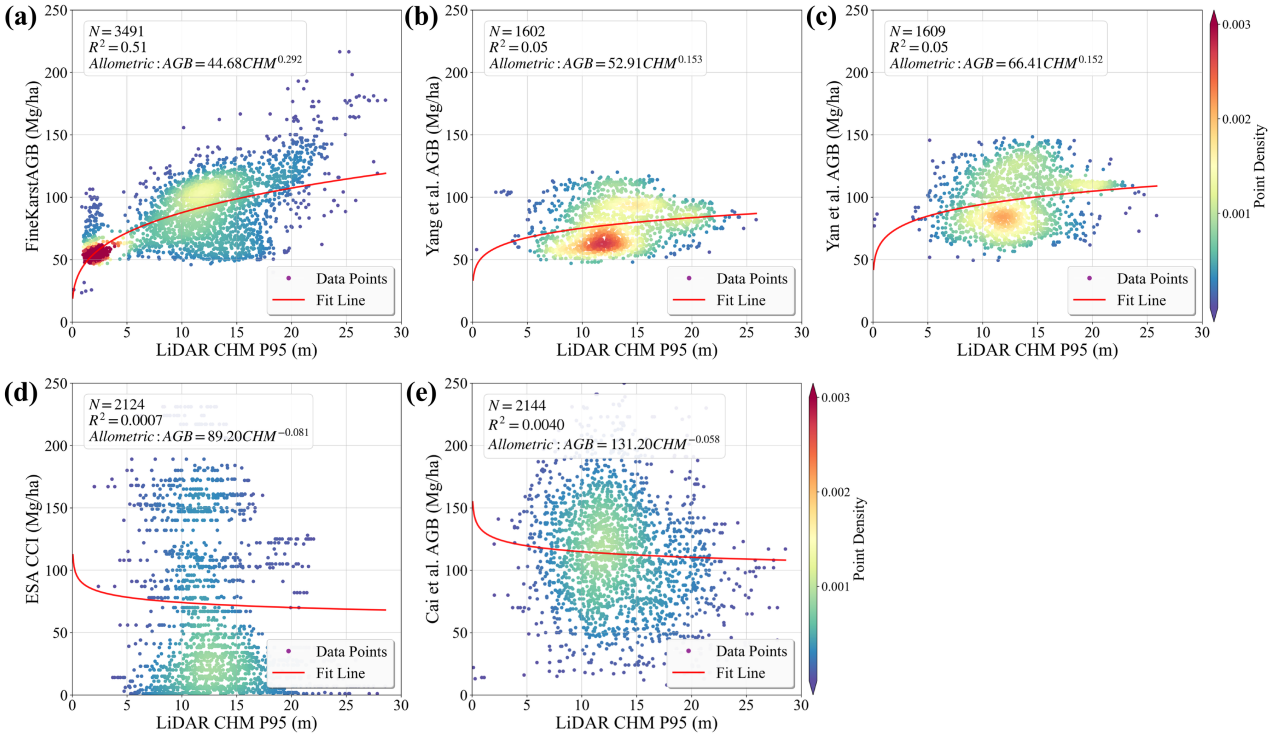


Figure S8. Structural-consistency assessment of the AGB datasets against the 95th percentile of UAV LiDAR-derived canopy height. Results are shown for (a) FineKarstAGB, (b) Yang et al. (2023), (c) Yan et al. (2023a), (d) ESA CCI (Santoro and Cartus, 2025), and (e) Cai et al. (2024b).

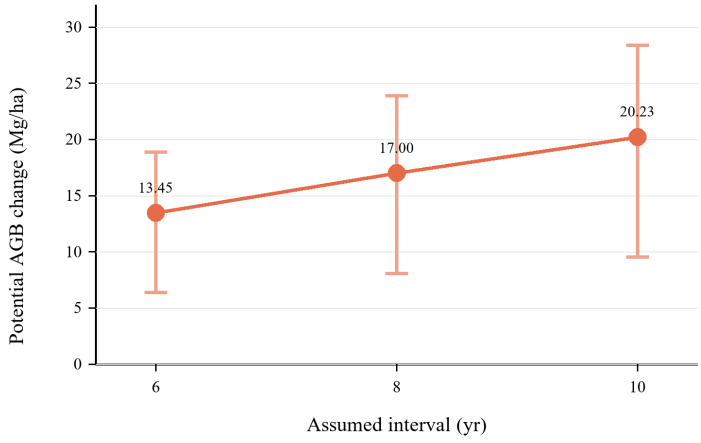


Figure S9. Potential median AGB changes estimated under assumed intervals of 6, 8, and 10 years; error bars indicate the interquartile range. These values are sensitivity scenarios rather than direct updates of the NFI labels.

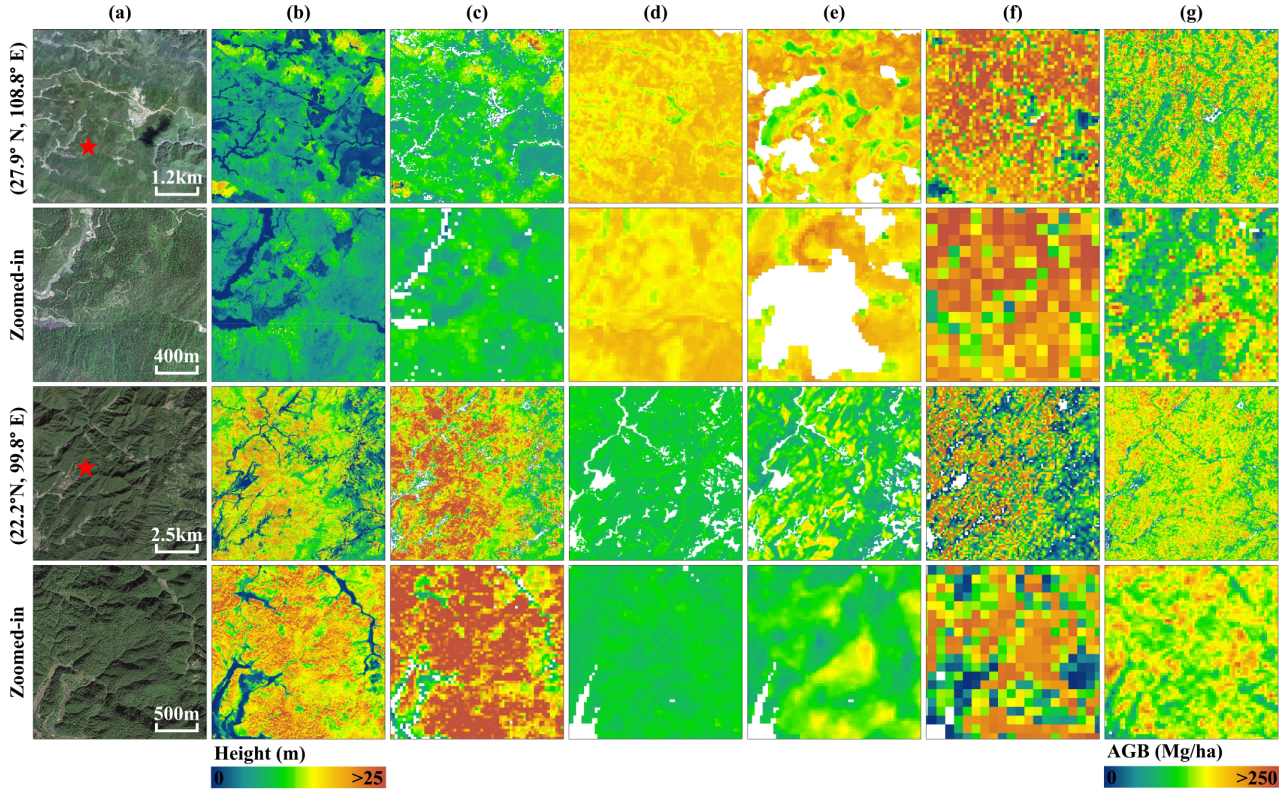


Figure S10. Illustration of typical scenarios and local details showing differences between FineKarstAGB and comparison AGB datasets. The red five-pointed stars in the GaoFen overview panels indicate the locations of the corresponding local details shown in the rows immediately below. (a) GaoFen imagery, (b) canopy height, (c) FineKarstAGB, (d) Yang et al. (2023), (e) Yan et al. (2023a), (f) ESA CCI (Santoro and Cartus, 2025), and (g) Cai et al. (2024b).

References

Cai, Y., Xu, X., Zhu, P., Nie, S., Wang, C., Xiong, Y., and Liu, X.: Unveiling Spatiotemporal Tree Cover Patterns in China: The First 30 m Annual Tree Cover Mapping from 1985 to 2023, ISPRS Journal of Photogrammetry and Remote Sensing, 216, 240–258, https://doi.org/10.1016/j.isprsjprs.2024.08.001, 2024a.

Cai, Y., Zhu, P., Xu, X., Li, X., Zhang, H., Nie, S., Wang, C., Wang, J., Shen, Q., Li, B., Wu, C., Liu, X., and Chen, Y.: CFATD: The First High-Spatiotemporal-Resolution Mapping of Forest Aboveground Biomass in China from 1985 to 2023 (Part VI: 2022-2023), https://doi.org/10.5281/zenodo.12747329, 2024b.

Cai, Y., Zhu, P., Li, X., Liu, X., Chen, Y., Shen, Q., Xu, X., Zhang, H., Nie, S., Wang, C., Wang, J., Li, B., Wu, C., and Zhuang, H.: Dynamics of China's Forest Carbon Storage: The First 30 m Annual Aboveground Biomass Mapping from 1985 to 2023, Earth System Science Data, 17, 6993–7018, https://doi.org/10.5194/essd-17-6993-2025, 2025.

Jian, N., Zhao, H., and Liu, M.: Driving Force and Potential of Forest Resource Change: Based on the Results of the Ninth National Forest Resources Inventory, Journal of Forestry and Grassland Policy, 2, 64–71, https://doi.org/10.12344/lczcyj.2022.09.22.0001, 2022.

Lang, N., Jetz, W., Schindler, K., and Wegner, J. D.: A High-Resolution Canopy Height Model of the Earth, Nature Ecology & Evolution, 7, 1778–1789, https://doi.org/10.1038/s41559-023-02206-6, 2023.

Liu, X., Su, Y., Hu, T., Yang, Q., Liu, B., Deng, Y., Tang, H., Tang, Z., Fang, J., and Guo, Q.: Neural Network Guided Interpolation for Mapping Canopy Height of China's Forests by Integrating GEDI and ICESat-2 Data, Remote Sensing of Environment, 269, 112 844, https://doi.org/10.1016/j.rse.2021.112844, 2022b.

Potapov, P., Li, X., Hernandez-Serna, A., Tyukavina, A., Hansen, M. C., Kommareddy, A., Pickens, A., Turubanova, S., Tang, H., Silva, C. E., Armston, J., Dubayah, R., Blair, J. B., and Hofton, M.: Mapping Global Forest Canopy Height through Integration of GEDI and Landsat Data, Remote Sensing of Environment, 253, 112 165, https://doi.org/10.1016/j.rse.2020.112165, 2021.

Santoro, M. and Cartus, O.: ESA Biomass Climate Change Initiative (Biomass_cci): Global Datasets of Forest above-Ground Biomass for the Years 2007, 2010, 2015, 2016, 2017, 2018, 2019, 2020, 2021 and 2022, v6.0, https://doi.org/10.5285/95913FFB6467447CA72C4E9D8CF30501, 2025.

Yan, S., He, G., and Zhang, X.: Forest Aboveground Biomass Products in China, 2013-2021, https://doi.org/10.57760/sciencedb.07122, 2023a.

Yang, Q., Niu, C., Liu, X., Feng, Y., Ma, Q., Wang, X., Tang, H., and Guo, Q.: Mapping High-Resolution Forest Aboveground Biomass of China Using Multisource Remote Sensing Data, GIScience & Remote Sensing, 60, 2203 303, https://doi.org/10.1080/15481603.2023.2203303, 2023.

Zhang, X., He, G., Yan, S., Long, T., Peng, X., Zhang, Z., and Wang, G.: Forest Status Assessment in China with SDG Indicators Based on High-Resolution Satellite Data, International Journal of Digital Earth, 16, 1008–1021, https://doi.org/10.1080/17538947.2023.2190625, 2023.